ADVANCED FUNCTIONAL MATERIALS
www.afm-journal.de

# Design of Visualized Ratiometric Mechanoluminescent Materials for High-Resolution Pressure Sensing

*Pengfei Zhang, Yuanting Wu,* Ziyi Guo, Yunmei Song, Jingyue Hu, Haojin Liu, and Lei Zhao**

**Optical sensing technology based on mechanoluminescent (ML) materials offers advantages such as rapid response, real-time monitoring, visual signal output, and multi-functional sensing, making it promising for various applications. However, traditional sensing techniques based on the absolute intensity of ML suffer from issues of low accuracy and large errors, which have a significant impact on the reliability and visual effectiveness of the sensor. To address these problems, this study employs a ratiometric ML pressure sensing method. By utilizing the primary color recognition of human cone cells, transition metal ion $Mn^{2+}$ and rare earth ion $Tb^{3+}$ are selected as luminescent centers. The rich intermediate colors ensure a wide range of colors that are easily distinguishable by the human eye. Through studies involving mechanical stimulation and similar high-energy radiation, it is confirmed that the differences in sensitivity between rare earth ions and transition metal ions, as well as the contributions of shallow trap states, are the reasons for the dynamic changes in the ratiometric ML intensity. Finally, a conceptual application of pressure sensing is realized by combining homogeneous gas compression with pipeline monitoring for dynamic visualization, self-referencing, and high-precision mechanical sensing.**

## 1. Introduction

ML materials represent a distinct class of substances that transform mechanical stimulation or deformation into light energy. Compared to traditional electrical signal sensing technologies, ML-based optical sensing offers several inherent advantages, including rapid response times for real-time monitoring, self-powering capabilities, visual signal output, and multifunctional sensing. These benefits make ML materials highly suitable for a diverse array of applications such as stress sensing, structural crack monitoring, non-contact diagnostics, and wearable technology.[1–7] Notably, research in gas pressure sensing using ML materials has been limited in recent years. Gas-driven pressure or deformations provide more uniform and stable sensing signals, enhancing the accuracy of the output. Additionally, gas-driven systems demonstrate excellent adaptability and can function under extreme conditions, such as high temperatures, high pressures, or in the presence of hazardous gases. Moreover, challenges in gas-driven human-computer interaction, such as precise control over gas flow and pressure and the development of reliable gas-driven systems, present opportunities for further exploration through the integration of ML materials.[8,9]

In previous studies, researchers have significantly advanced the field by enhancing the conversion efficiency of ML materials and laying the foundation for quantitative analyses through the integration of various ML materials with organic molecules to construct sensor devices.[10–13] However, these studies have predominantly relied on mechanical stimulation parameters for calibrating absolute ML intensity to characterize sensors, introducing several accuracy-related shortcomings. First, this method is susceptible to interference from other optical signals. Second, the variability of local environmental conditions such as temperature, humidity, and corrosive substances tends to exacerbate these issues. Additionally, the single ML in bright field environments is challenging to visualize, leading to issues of insufficient accuracy, significant errors, and lack of visualizability in optical sensing technology based on absolute ML intensity.[14,15] These issues significantly compromise the reliability and visual quality of optical sensing technologies. Recent advancements have shown that fluorescence intensity ratio sensing technology, which utilizes the synergy of different luminescence centers, effectively addresses the challenges of accuracy in absolute intensity sensing, particularly in up/down conversion temperature sensing.[16,17] Consequently, employing ratiometric ML intensity sensing can mitigate the aforementioned problems. This approach is less influenced by external environmental factors, thereby providing more sensitive and stable stress-sensing outputs. Additionally, incorporating multiple luminescent

P. Zhang, Y. Wu, J. Hu
School of Materials Science and Engineering
Shaanxi University of Science and Technology
Xi'an 710021, P. R. China
E-mail: wuyuanting@sust.edu.cn
Z. Guo, Y. Song, H. Liu, L. Zhao
School of Physics and Opto-Electronic Technology
Collaborative Innovation Center of Rare-Earth Optical Functional Materials and Devices Development
Baoji University of Arts and Sciences
Baoji, Shaanxi 721016, P. R. China
E-mail: zhaoleibjwl@163.com

The ORCID identification number(s) for the author(s) of this article can be found under https://doi.org/10.1002/adfm.202412911

DOI: 10.1002/adfm.202412911

 

centers in the ratio-based sensing scheme enhances visual detection by the naked eye. In 2021, Wang et al. achieved stress/strain-induced ML color manipulation in the $Sr_2P_2O_7$ system by introducing two different luminescent centers, $Eu^{2+}/Eu^{3+}$, enabling semi-quantitative visual mechanical sensing through highly reliable ML color changes.[18] In 2022, Wang et al. designed a series of dual-activator phosphate materials to realize ratiometric ML sensing and established an evaluation system to quantify the stress-sensing performance of these ratiometric ML materials.[19] In 2024, Wang et al. proposed a versatile approach that manipulates the threshold of ML materials via a multi-layer flexible composite structure to achieve ratiometric ML for stress-visualized quantitative detection.[20] These studies provide valuable insights for ongoing research, addressing some issues encountered in absolute intensity-based sensing techniques. However, due to the spectral overlap of the dual activators and the narrow emission spectrum distance, significant color changes for visualization were not achieved. Additionally, constructing multi-layer structure ratiometric ML sensors with different doped ML materials is cumbersome. Therefore, based on the human eye's three different cone cells, where the first discriminant color is red and the second discriminant color is green, we selected transition metal ions $Mn^{2+}$ and rare earth ions $Tb^{3+}$ as the luminescence centers of the nonpiezoelectric material $\beta$-$Ca_3(PO_4)_2$ host.[21,22] Notably, $\beta$-$Ca_3(PO_4)_2$ belongs to the R3c space group and is classified as a nonpiezoelectric material. Calcium exhibits a diverse range of coordination environments, offering excellent tunability when introducing different luminescent centers at various lattice sites, thereby meeting the need for dynamic color changes. Additionally, spectral separation and dynamic color differences ensure a sufficient range of colors recognizable by the human eye, ultimately achieving self-referencing, high-precision mechanical sensing based on ML intensity ratios, and dynamic visualization of luminescent colors.

In this work, we successfully developed a high-resolution visual ratiometric ML sensing technique in $\beta$-$Ca_3(PO_4)_2$ (CPO): $Tb^{3+}$, $Mn^{2+}$. The presence of sensitivity differences was proved using similar high-energy X-ray excitations and mechanical stimuli. Sensor devices were then encapsulated, and the visualization of ratiometric ML under tension and friction stimulation was studied. Subsequently, the reliability mechanism of the CPO: $Tb^{3+}$, $Mn^{2+}$@PDMS composite device was investigated through dynamic spectral and trap distribution studies under frictional electrical and X-ray excitations. Finally, the CPO: $Tb^{3+}$, $Mn^{2+}$@PDMS composite device was utilized for visualized ratio-based sensing in the field of pressure sensing. This strategy provides a new approach for designing novel visualized pressure sensing.

## 2. Results and Discussion

### 2.1. Design Concept of a Visual Gas Pressure Sensor Device

The design concept of the gas pressure intensity ratio sensor component involves selecting suitable luminescent centers, understanding the sensing mechanism, optimizing the optical setup, and applying data analysis and calibration methodologies. Initially, luminescent center colors are chosen based on the first and second recognition colors of human cone cells, which are red and green, respectively. Consequently, the transition metal ion $Mn^{2+}$ and the rare-earth ion $Tb^{3+}$ are selected as luminescent centers. This choice ensures a color range distinguishable by the human eye. Additionally, the difference in luminescent properties between rare earth and transition metal ions can induce dynamic color changes under strain. These two factors combined may result in a dynamic ML process under pressure (**Figure 1a**). As shown in Figure 1b, we conducted experiments using a syringe-connected tube furnace pressure gauge as the gas pressure triggering and monitoring device (Figure S1, Supporting Information). The syringe was pushed from the 100 cc mark to the 10 cc mark, and the manometer displayed a scale of 0–0.12 MPa (Video S1, Supporting Information). The CPO: $Tb^{3+}$, $Mn^{2+}$@PDMS composite device was tested on top of the syringe. In agreement with the hypothesis in Figure 1a, the device exhibited high-resolution dynamic visual ML emission from green to red during the expansion process, with intermediate colors including yellow and orange (Figure 1c; Video S2, Supporting Information). Figure S1b (Supporting Information) displays the ML spectral graph under dynamic pressure changes. As gas pressure increases, both the intensity and integrated area of the $Mn^{2+}$ luminescent center increase significantly in the dynamic spectra. Considering the self-calibrating characteristics of the intensity ratio sensing in extreme environments, we examined the sensitivity and accuracy of this sensing method for wavelengths of 544 nm ($Tb^{3+}$) and 651 nm ($Mn^{2+}$) under dynamic pressure (Figure 1d). As the pressure rose from 0 to 0.12 MPa, the $I_{Tb}/I_{Mn}$ intensity ratio decreased from 6.235 to 1.17. We performed an exponential fit on the intensity ratio across different gas pressures, yielding the equation $y = 6.9147e^{(x/-0.0543)}$, where x is the gas pressure from syringe compression and y is the $I_{Tb}/I_{Mn}$ intensity ratio. The goodness-of-fit was exceptionally high at 99.96%. These results underscore the ultra-high sensitivity and accuracy of the CPO: $Tb^{3+}$, $Mn^{2+}$@PDMS composite device, highlighting its potential for real-time, high-resolution visual monitoring of dynamic, especially in novel visualized pressure sensing.

### 2.2. Feasibility Analysis of Sensor Device

First, a sensor component was designed by doping the rare earth ion $Tb^{3+}$ and the transition metal ion $Mn^{2+}$ into the $\beta$-$Ca_3(PO_4)_2$ host lattice. According to Figure S2 (Supporting Information), the phase structures of CPO: $Tb^{3+}$ and CPO: $Mn^{2+}$ ML phosphors match the standard $Ca_3(PO_4)_2$ structure (JCPDS #70-2065). The series of emission spectra determines that the concentration quenching points of CPO: $x$$Tb^{3+}$ and CPO: $x$$Mn^{2+}$ are 50% and 15%, which are respectively attributed to the $^5D_4 \rightarrow {}^7F_5$ transition of $Tb^{3+}$ ions and $^4T_1 \rightarrow {}^6A_1$ radiative transition of $Mn^{2+}$ ions (Figure S3, Supporting Information). Given the broad spectral range of $Mn^{2+}$ ions, CPO: $Tb^{3+}$@PDMS and CPO: $Mn^{2+}$@PDMS were selected for encapsulating the sensor devices, respectively.

The strain-dependent ML spectra, shown in Figure S4 (Supporting Information), indicate that the ML emission intensity of $Tb^{3+}$ and $Mn^{2+}$ ions increases with tensile strain. Normalizing the intensities of the $^5D_4 \rightarrow {}^7F_5$ and $^4T_1 \rightarrow {}^6A_1$ transitions

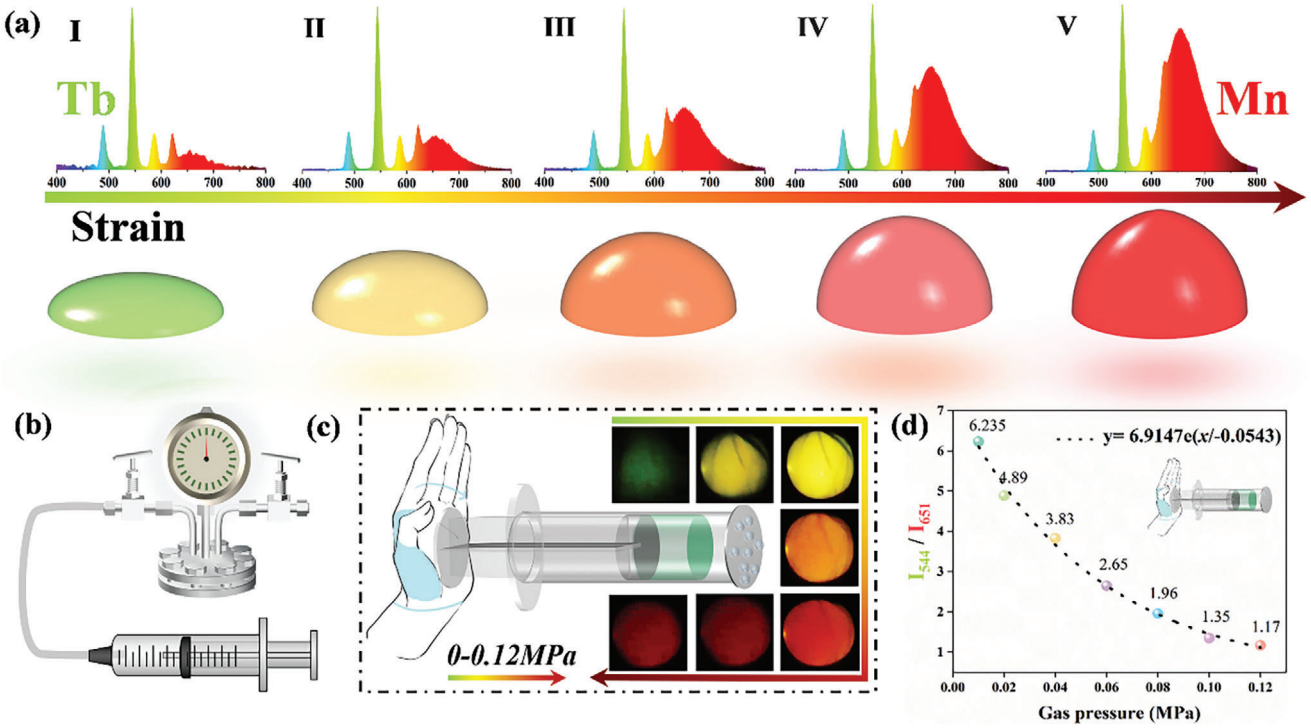


**Figure 1.** a) Schematic diagram of gas sensing based on ML (mechanoluminescence) intensity ratio (from left to right indicating increasing gas pressure). b) Diagram of the syringe-type pressure measurement device. c) Photographs of the ML from the syringe-driven CPO:0.5$Tb^{3+}$, 0.01$Mn^{2+}$@PDMS composite device under different gas pressures (0–0.12 MPa). d) Intensity ratio ($I_{Tb}/I_{Mn}$) and sensor function fitting at different gas pressures.

under 20% strain demonstrates that the ML intensity exhibits a linear response to strain (**Figure 2a**). The fitting functions for the CPO: 0.50$Tb^{3+}$@PDMS and CPO: 0.01$Mn^{2+}$@PDMS composite devices are $y = 0.229x$-3.383 and $y = 0.051x$+0.053, respectively, with goodness-of-fit values of 99.7% and 99.1%. The dynamic strain ML images in Figure 2b, corresponding to the spectral data, show increased emission intensity and area with increasing tensile strain, meeting the requirements for visual sensing. It is worth noting that the growth rate of the CPO: 0.01$Mn^{2+}$@PDMS composite device is significantly higher than that of the CPO: 0.50$Tb^{3+}$@PDMS device, which represents the possibility of achieving ratiometric ML changes after the introduction of dual luminescent centers and the possibility of achieving a visualized change from green to red with the naked eye.

Based on the principle that high-energy electron bombardment is similar to the ML radiation path proved by Wang et al.,[23] we used X-ray excitation (RL) as an alternative high-energy excitation method to mechanical stimulation response. As depicted in Figure 2c and Figure S5 (Supporting Information), following the initiation of a fixed dose, the RL intensity increases rapidly and stabilizes within 1 s. Subsequently, the RL intensity of CPO: 0.50$Tb^{3+}$ gradually decreases, while that of CPO: 0.01$Mn^{2+}$ increases until the X-rays are turned off. The reason for this phenomenon may be different radiation efficiency. Figure S6 (Supporting Information) gives the estimation of the X-ray light yield of the CPO: 0.5$Tb^{3+}$ and CPO: 0.01$Mn^{2+}$ under steady-state X-ray illumination, with CsI: TI as the reference sample. The estimated X-ray light yields (steady-state) for CPO: 0.50$Tb^{3+}$ and CPO: 0.01$Mn^{2+}$ were 9794 and 36 067 photons per MeV, respectively. The nearly fourfold increase in light yield of CPO: 0.01$Mn^{2+}$ suggests that X-ray excitation more efficiently excites $Mn^{2+}$, leading to an increase in its RL. Additionally, the enhancement of dynamic $RL_{Mn}$ may be attributed to the contribution of traps. As shown in Figure S7b (Supporting Information), after UV excitation, there is a continuous distribution of traps between 300 and 500 K. However, after high-energy X-ray excitation, the trap density significantly increases at 300–400 K. Consequently, under high-energy excitation, these traps are continuously filled and rapidly released through radiative transitions, leading to increased intensity. This indicates that the presence of shallow traps contributes to the enhancement of red emission in CPO: $Mn^{2+}$.[24–26] Figure 2d provides RL spectra for fixed doses excited for 1 and 60 s, with the change from $I_{Tb}$ being greater than $I_{Mn}$ to $I_{Tb}$ being less than $I_{Mn}$, It is further confirmed that under high-energy excitation, the co-doped device CPO: $Tb^{3+}$, $Mn^{2+}$@PDMS is expected to achieve ratiometric ML changes and dynamic color visualization processes. Finally, Figure 2e,f and Figure S8 (Supporting Information) employ the Vienna Ab Initio Simulation Package (VASP) for Density Functional Theory (DFT) simulations, where the O orbitals dominate the valence band maximum (VBM) and the Ca orbitals contribute mainly to the conduction band minimum (CBM). With the introduction of $Mn^{2+}$ dopants into the matrix, the overall projected density of states (PDOS) of the host materials remains largely unaffected (Figure 2f). The $Mn^{2+}$ states are primarily located within the bandgap.[27] Compared to the band gap of the CPO matrix, the introduction of Mn ions in CPO: 0.015$Mn^{2+}$ leads to multiple impurity states

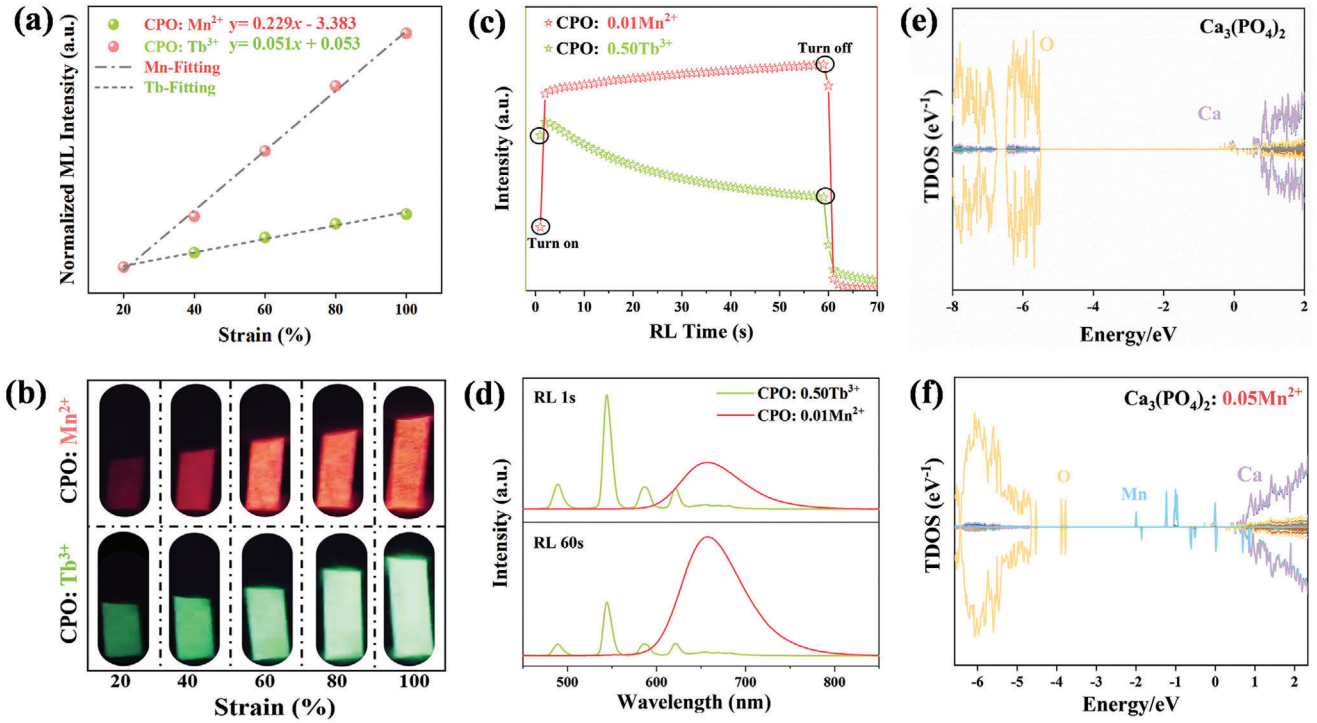


**Figure 2.** a) Normalized ML intensity of CPO:0.5$Tb^{3+}$@PDMS and CPO: 0.01$Mn^{2+}$@PDMS under different strains. b) Dynamic ML photographs of CPO:0.5$Tb^{3+}$@PDMS and CPO: 0.01$Mn^{2+}$@PDMS under different strains. c) Continuous collection of the RL intensity for CPO:0.5$Tb^{3+}$ and CPO: 0.01$Mn^{2+}$ at a fixed dosage. d) RL spectra for a fixed dosage excited for 1s and 60s. e) TDOS diagram of CPO. f) TDOS diagram for CPO: 0.05$Mn^{2+}$.

appearing in the bandgap. It is hypothesized that the high strain sensitivity of CPO: 0.015$Mn^{2+}$ may also arise from the contribution of impurity states introduced by the $Mn^{2+}$ ions.

### 2.3. Structural Characterization of Sensor Devices

After confirming that the difference in radiative rates under high-energy excitation and the compensation of traps contribute to self-calibrated intensity ratio strain sensing, we synthesized CPO: 0.5$Tb^{3+}$, $x$$Mn^{2+}$ with varying concentrations of $Mn^{2+}$ ions ($x$ = 0.01, 0.05, 0.10, 0.15, 0.20) using the high-temperature solid-state method. As the $Mn^{2+}$ doping concentration increased, the transition intensity of ($4T_1 \rightarrow 6A_1$) also increased, causing the luminescent color of the sample to shift from green to red under ultraviolet excitation (Figure S9, Supporting Information). Considering the high strain sensitivity of $Mn^{2+}$ ions and the need for a broad visual color range under high strain, we selected the photo-induced green luminescent CPO: 0.5$Tb^{3+}$, 0.01$Mn^{2+}$@PDMS composite device to study its ML performance under tension and friction.

The phase structure and device composite process flowchart are illustrated in Figure S10 (Supporting Information). Here, it is observed that the $\beta$-$Ca_3(PO_4)_2$ structure is hexagonal, with calcium atoms in five coordination sites and phosphorus atoms in one site, forming tetrahedral coordination with four oxygen atoms. The absence of impurity diffraction peaks in the $\beta$-$Ca_3(PO_4)_2$ matrix was confirmed through GSAS refinement, achieving a low R-value. The preparation of the CPO: $Tb^{3+}$, $Mn^{2+}$@PDMS composite device involved magnetically stirring the organic–inorganic materials and annealing them to form the final product. XRD analysis confirmed that the diffraction peaks of the CPO: 0.5$Tb^{3+}$, 0.01$Mn^{2+}$@PDMS composite were consistent with the standard $\beta$-$Ca_3(PO_4)_2$ structure (JCPDS #70-2065), with the broad amorphous diffraction peak of PDMS also present. Subsequent morphological and energy spectrum analyses of the cross-sections of the CPO: $Tb^{3+}$, $Mn^{2+}$, and CPO: $Tb^{3+}$, $Mn^{2+}$@PDMS devices were performed (Figure S11, Supporting Information). The CPO: $Tb^{3+}$, $Mn^{2+}$ morphology comprised amorphous particles ranging from 1 to 20 μm in size. The CPO: $Tb^{3+}$, $Mn^{2+}$@PDMS device had a thickness of ≈755 μm, with CPO: $Tb^{3+}$, $Mn^{2+}$ uniformly distributed within the PDMS matrix. Energy-dispersive spectroscopy and elemental mapping of the circular area (Figure S10h, Supporting Information) confirmed the uniform distribution of Ca, P, O, Tb, and Mn, indicating successful incorporation of $Tb^{3+}$ and $Mn^{2+}$ ions. Additionally, we have provided images of the device used for subsequent tests, as shown in Figure S12 (Supporting Information). Due to the insufficient clamping force of the pneumatic grips in the tensile strain experiment and the sharpness of the probe in the friction experiment, we had to use relatively thicker devices for characterization. However, in the pressure-sensing characterization experiment, the pressure from the syringe was not sufficient to drive the thicker film. Therefore, thinner devices were selected for the corresponding characterization.

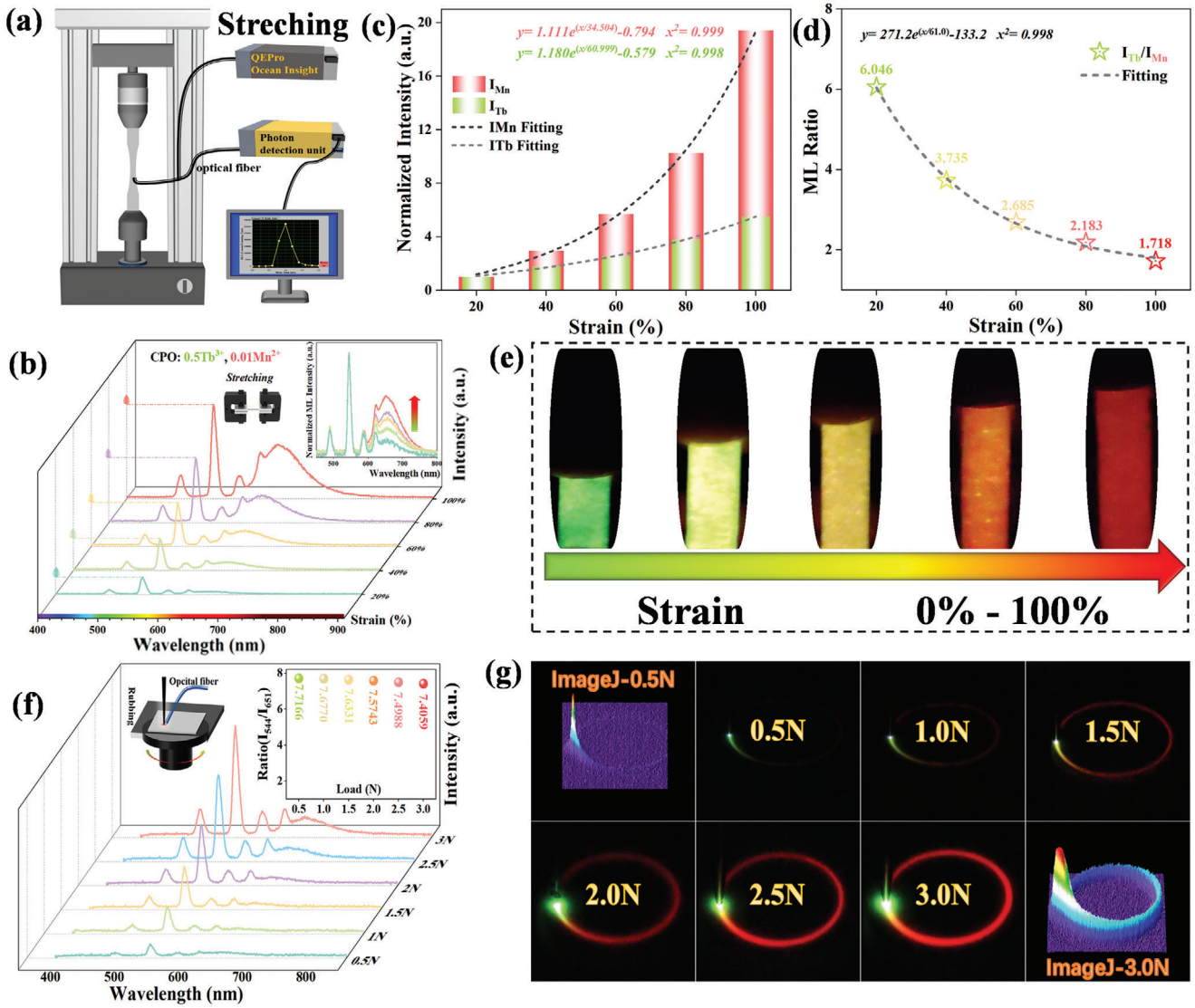


**Figure 3.** a) Schematic diagram of the stretching device for the composite sensor. b) ML spectra of CPO: 0.5Tb$^{3+}$, 0.01Mn$^{2+}$@PDMS composite device under different strains. c) Variation trend of ITb and IMn integrated strength of CPO: 0.5Tb$^{3+}$, 0.01Mn$^{2+}$@PDMS composite devices under different travel strains. d) Variation trend of $I_{Tb}/I_{Mn}$ of CPO: 0.5Tb$^{3+}$, 0.01Mn$^{2+}$@PDMS composite devices under different travel strains. e) ML photographs of CPO: 0.5Tb$^{3+}$, 0.01Mn$^{2+}$@PDMS composite device under different strains. f) M spectra of CPO: 0.5Tb$^{3+}$, 0.01Mn$^{2+}$@PDMS composite device under different frictional forces, the inset shows a schematic diagram of the friction device. g) ML photographs of CPO: 0.5Tb$^{3+}$, 0.01Mn$^{2+}$@PDMS composite device under different frictional forces, the ML photographs at 0.5 and 3N have been processed with ImageJ software.

### 2.4. Self-Calibrated Sensing of Sensor Device Under Multimodal Stimulation

**Figure** 3a presents a schematic of the tensile testing setup, where the CPO: Tb$^{3+}$, Mn$^{2+}$@PDMS device is subjected to varying levels of strain using a tensile machine. A photon counter and an ocean optical spectrometer collect the optical signals. As the strain increases from 0% to 100%, the ML spectral intensities $I_{Tb}$ and $I_{Mn}$ in the CPO: 0.5Tb$^{3+}$, 0.01Mn$^{2+}$@PDMS device gradually increase (Figure 3b). The photon counter also found that as the strain increased to 100%, the number of photons gradually increased by nearly double (Figure S13, Supporting Information). By normalizing the initial intensity of the spectrum under different strains, it was found that $I_{Tb}$ and $I_{Mn}$ increased exponentially (Figure 3c), and the change rate of $I_{Mn}$ was also much higher than that of $I_{Tb}$, which was consistent with the previous results in Figure 2a. It is also evident from the ML photos that the ML color dynamically shifts from green to red, corresponding to the ML spectrum data (Videos S3 and S4, Supporting Information). Figure 3d presents the intensity ratio at different strains, showing a first-order exponential decrease as strain increases. The fitting function is $y = 271.2e^{(x/61.0)} - 133.2$, with a high goodness of fit of 99.8%, indicating the sensor's high sensitivity and accuracy. For pressure sensors, the actions applied to the sensor device are not limited to expansion and stretching. Consequently, we investigated the ML sensing characteristics under different

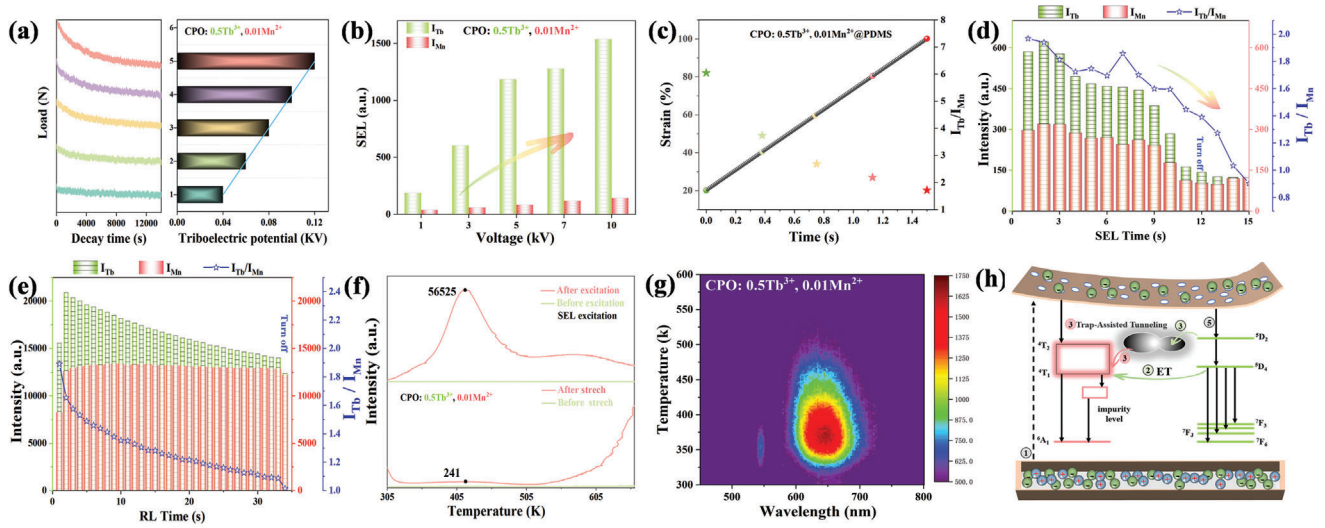


**Figure 4.** a) Depicts the triboelectric potential of the CPO: $0.5Tb^{3+}$, $0.01Mn^{2+}$@PDMS composite device under various strains, with the graph on the right showing the difference in triboelectric potential under different strains. b) Shows the changes in SEL intensity at 544 and 651 nm for the CPO: $0.5Tb^{3+}$, $0.01Mn^{2+}$ composite device under varying voltages. c) Relationship between time and ratio ML at different strains. d) changes in SEL intensity of $I_{Tb}$, $I_{Mn}$, and $I_{Tb}/I_{Mn}$ for the fixed-voltage CPO: $0.5Tb^{3+}$, $0.01Mn^{2+}$ composite device. e) Presents the variations in RL intensity of $I_{Tb}$, $I_{Mn}$, and $I_{Tb}/I_{Mn}$ for the CPO: $0.5Tb^{3+}$, $0.01Mn^{2+}$ composite device at a fixed dosage. f) Displays the 2D-Thermoluminescence spectra of the CPO: $0.5Tb^{3+}$, $0.01Mn^{2+}$@PDMS composite device before and after stretching and SEL excitation. g) 3D-Thermoluminescence of CPO: $0.5Tb^{3+}$, $0.01Mn^{2+}$. h) Offers a mechanistic diagram of the CPO: $0.5Tb^{3+}$, $0.01Mn^{2+}$@PDMS composite device.

friction loads. As shown in Figure 3f, the ML spectral intensity progressively rises with increasing friction load. The intensity ratio $I_{Tb}/I_{Mn}$ decreases from 7.7166 at 0.5 to 7.4059 at 3.0 N, as shown in the inset. Figure 3g shows the ML images of the CPO: $0.5Tb^{3+}$, $0.01Mn^{2+}$@PDMS device under different loads, where the ML at the contact points is primarily green emission from $Tb^{3+}$. It is worth noting that both the spectra and ML images predominantly feature emission from $Tb^{3+}$ ions. This is because the local friction experiment does not involve a continuous application of force; the force position is constantly changing, preventing the $Mn^{2+}$ luminescent centers from receiving trap compensation under high-energy stimulation. In contrast, the tensile process involves continuous high-energy stimulation in the same area, leading to significant changes in intensity ratio and dynamic ML color due to superior radiative differences and trap compensation.

### 2.5. Mechanism of Ratiometric ML Sensor Device

To gain a deeper understanding of the ML phenomenon and the intensity ratio sensing mechanism of the CPO: $Tb^{3+}$, $Mn^{2+}$@PDMS sensor device under force stimulation, we first demonstrated the mechanism of ML generation by studying the triboelectric potential under different friction forces. (**Figure** 4a). When the CPO: $Tb^{3+}$, $Mn^{2+}$@PDMS device is rubbed against PDMS, the matrix acquires electrons and develops a negative potential. Prompted by the resulting triboelectric field, the transferred electrons in the PDMS matrix can be accelerated to bombard the CPO: $Tb^{3+}$, $Mn^{2+}$@PDMS, potentially activating or exciting the luminescent centers.[23] As a result, the triboelectric potential difference increases with the force, enhancing the ML intensity. This process is analogous to SEL (Static electricity luminescence). As the static electricity voltage rises, the ML spectral intensities of the CPO: $0.5Tb^{3+}$, $0.01Mn^{2+}$@PDMS device gradually increase, indicating an effective radiative pathway under high-energy electron bombardment (Figure 4b; Figure S14, Supporting Information).

Subsequently, we utilized this high-energy excitation mechanism to further verify the dynamic color changes in ML under force stimulation through SEL and X-ray stimulation. As previously discussed, the prerequisite for ratiometric ML is sustained strain stimulation, which requires the application of force to a fixed position. As shown in Figure 4c, during the variation of strain from 20% to 100%, corresponding to a force application time of 0–1.5 s, a strong ratiometric ML change was achieved. In contrast, this effect was not observed during the friction process (Figure S15, Supporting Information). Therefore, the ratiometric ML mechanism should be further explored through continuous high-energy excitation. The results under fixed-dose X-ray excitation (Figure 4d,e; Figure S16, Supporting Information) show that the intensity ratio continuously decreases, consistent with the predictions in Figure 2c. This also confirms that the difference in radiation efficiency makes $Mn^{2+}$ more easily excited by X-rays, making it one of the reasons for the change in the ratio ML. It is noteworthy that this decrease in consistency indicates that under high-energy stimulation, SEL and RL have the same radiative pathway. In addition, the most important point we consider is to verify the role of trap-assisted in co-doped devices, the TL spectra before and after SEL and force stimulation were presented in Figure 4e, confirming the generation of numerous traps under high-energy excitation. By studying the 3D-thermoluminescence of CPO: $0.50Tb^{3+}$, $0.01Mn^{2+}$, it was found that most of the traps in the 300–530 K range were attributed to the red emission from $Mn^{2+}$ ions. This indicates that the carrier-assisted effect provided by these traps continuously enhances the

radiative transitions of $Mn^{2+}$ ions, making trap-assisted effects one of the reasons for the ratiometric ML changes.[28] In addition, As shown in Figure S17 (Supporting Information), the excitation and emission spectra reveal an overlapping peak ≈500 nm between the emission spectrum of CPO: $0.5Tb^{3+}$ and the excitation spectrum of CPO: $0.01Mn^{2+}$. Monitoring the lifetime at 547 nm in CPO: $0.5Tb^{3+}$, $0.01Mn^{2+}$ samples shows a decrease in lifetime from 1.46 to 0.81 ms, indicating that energy transfer occurs between $Tb^{3+}$ and $Mn^{2+}$. Therefore, energy transfer may also be one of the reasons for the changes in ratiometric ML. Finally, a referenced mechanism diagram is shown in Figure 4f. Under force stimulation, electrons are excited to the conduction band and then participate in radiative transitions of $Tb^{3+}$ and $Mn^{2+}$ ions, producing ML. During the continuous stress process, a portion of the carriers are stored in the traps created, mainly dominated by defects in CPO: $0.01Mn^{2+}$ (Figure 4g). This leads to continuous tunneling to the energy levels of $Mn^{2+}$ ions, additionally, the energy transfer between $Tb^{3+}$ and $Mn^{2+}$, along with the excellent radiative efficiency of Mn ions, further enhances the emission of $Mn^{2+}$ ions in the ML.

### 2.6. Applications of Ratiometric ML Gas Sensor Device

The above data confirm that the CPO: $Tb^{3+}$, $Mn^{2+}$@PDMS composite sensor device is fully capable of achieving ratiometric ML intensity changes during sustained strain, featuring dynamic color visualization and self-referencing characteristics. Therefore, we designed a pressure monitoring system for fracture points in gas pipelines, focusing on the relatively uniform strain produced by gas pressure, which more accurately highlights the ratiometric ML changes in the device. Previously, we recognized that the repeatability and reproducibility of ML devices are crucial for practical applications.[29,30] In a continuous 300 s repeatability test (stretching speed of four times per second, with 50% deformation), it was observed that the initial stretching intensity of $I_{Tb}$ and $I_{Mn}$ was the highest, followed by a gradual decay. Notably, the ML intensity of $I_{Tb}$ stabilized ≈560, while $I_{Mn}$ stabilized ≈660 (**Figure** 5a,b). At these intensity levels, the device can still be used for pressure-sensing research, demonstrating its excellent repeatability. In Figure 5c, we observe that ML intensity decreases significantly as the number of stretching cycles increases. This phenomenon has been carefully studied in previous work and is due to the reduced bonding strength between PDMS and the ML material during stretching, leading to a decrease in ML intensity. After self-recovery for 18 h and heating for 6 h, the ML intensity recovered to 84.8% of its initial value, further demonstrating the material's recoverability.[31] To determine whether the material can recover to its initial state after stretching, we conducted stress-strain curves and XRD analyses before and after stretching (Figure S18, Supporting Information). The stress-strain curves show that the elastic modulus decreases slightly, while the XRD data remain unchanged before and after stretching. In addition, we give the advantages compared with other sensor devices in Table S1 (Supporting Information).[32] These results demonstrate that the ML device has excellent sensing reproducibility and repeatability.

As illustrated in Figure 5f, the CPO: $Tb^{3+}$, $Mn^{2+}$@PDMS device is positioned on a PTFE pipe with a crack, one end sealed and the other connected to an air pump. When the air pump is activated, the pressure increases, and only the area with the crack in the CPO: $Tb^{3+}$, $Mn^{2+}$@PDMS device deforms, leading to a rapid color transition from green to red (Figure 5d). An external fiber optic cable collects the ML signal and transmits it to a spectrometer, allowing strain or mechanical data to be acquired via a computer (Figure 5e). Additionally, a camera monitoring system at the external end enables leak detection and alert systems. This device is particularly effective for detecting gas pressure imbalances, as the mechanical information at the imbalance points can be estimated at any time through visualized ratiometric ML. This provides a new approach for the practical application of ratiometric ML.

## 3. Conclusion

In summary, we have successfully developed a ratiometric dual activator phosphor for high-resolution visual strain sensing. First, by considering the primary color recognition of human eye cone cells, we introduced rare-earth/transition metal ion doping into the nonpiezoelectric matrix $\beta$-$Ca_3(PO_4)_2$. High-energy radiation demonstrated that trap-assisted effects and differences in radiative efficiency could potentially lead to the realization of ratiometric ML. We conducted a detailed study on the sensing performance of the CPO: $Tb^{3+}$, $Mn^{2+}$@PDMS device under strain and friction mechanical responses and found that the intensity ratio $I_{Tb}/I_{Mn}$ exhibited a wide range of changes under continuous strain, enabling precise, visualized color changes, making it suitable as an accurate sensor device. Subsequently, through high-energy excitation and trap studies, we further confirmed that the primary reasons for ML color changes in the dual-activator system were trap assistance, differences in radiative efficiency, and energy transfer. As a conceptual application demonstration, we simulated the imbalance monitoring and real-time monitoring process of gas pressure and showed the excellent repeatability and reproducibility of the device's continuous operation. This provides new ideas for the future development of ratiometric ML visualization sensing applications.

## 4. Experimental Section

*Synthesis of Inorganic Material Sources*: The phosphor samples were synthesized by solid-state reaction with reagents $CaCO_3$ (99%), $(NH_4)_2HPO_4$ (99%), $Tb_4O_7$ (99.99%) and $MnCO_3$ (99.99%) as raw materials. Stoichiometric mixtures with the composition $Ca_3(PO_4)_2$: $xTb^{3+}$ ($x$ = 0.20, 0.30, 0.40, 0.50, 0.60), $Ca_3(PO_4)_2$: $xMn^{2+}$ ($x$ = 0.01, 0.05, 0.10, 0.15, 0.20) and $Ca_3(PO_4)_2$:$0.5Tb^{3+}$, $0.01Mn^{2+}$ were mixed homogeneously in an agate mortar and subsequently moved to alumina crucibles, presinter at 400 °C for 3 h in a muffle furnace, then sinter at 1300 °C for 12 h under a reducing atmosphere (90 $H_2$/10 $N_2$). After the product was cooled to room temperature, it was ground into fine powder. In the article, the abbreviation "CPO" is used to refer to $Ca_3(PO_4)_2$.

*Construction of Composite Sensor Device*: Polydimethylsiloxane (PDMS) acts as an elastic matrix to provide internal stress to the ML powder (Sylgard 184, Dow Corning). First, grind the powder in an agate mortar for a few minutes to obtain more uniform particles. Second, 10 g of PDMS base resin and 1 g of curing agent were mixed in a disposable cup. Add a magnet and stir on a stimulating stirrer for half an hour. Finally, pour the stirred mixture into a homemade glass grinding tool and solidify at 80 °C for 2 h to obtain a PDMS-based ML elastomer.

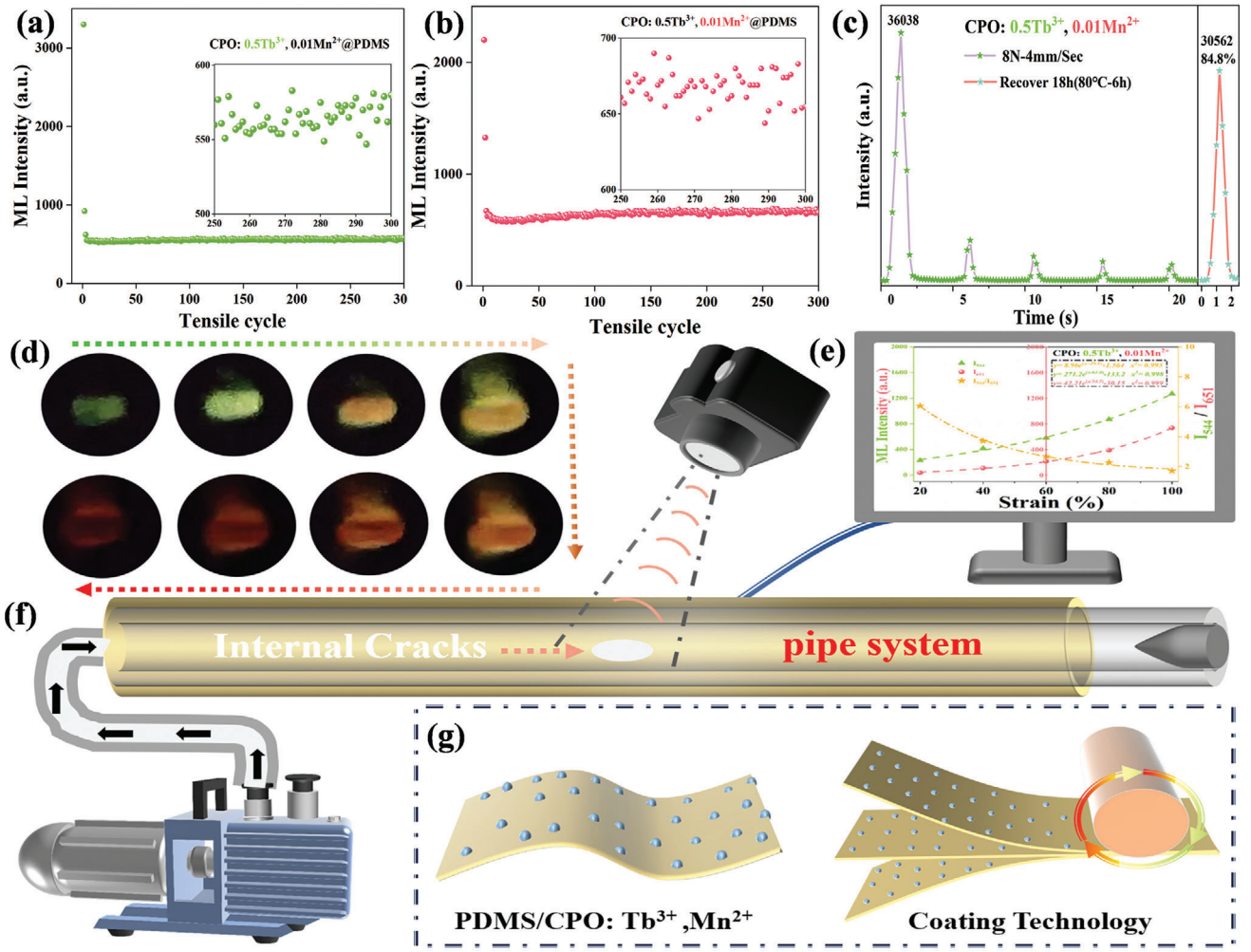


**Figure 5.** Repeatability test of CPO: $0.5Tb^{3+}$, $0.01Mn^{2+}$@PDMS device stretched for 300s. a) $I_{Tb}$. b) $I_{Mn}$. c) Self-recovery test. d) Dynamic pressure monitoring ML photo of CPO: $0.5Tb^{3+}$, $0.01Mn^{2+}$@PDMS composite device. e) Real-time data acquisition via computer and round-the-clock camera monitoring. f,g) Schematic design of the gas leak pipeline apparatus, assisted by an air pump, with the outer layer encapsulating the composite CPO: $0.5Tb^{3+}$, $0.01Mn^{2+}$@PDMS pressure sensor device.

*Characterizations*: The X-ray diffraction (XRD) patterns were recorded on Germany Brucker D2 PHASER with Cu K$\alpha$ radiation ($\lambda$ = 1.58184 Å) in the 2$\theta$ range of 10–80° equipped at 40 kV and 40 mA. The phase parameter was refined by the Rietveld method using the General Structure Analysis System (GSAS) program. The crystal structure is drawn using diamond software. The photoluminescence (PL), photoluminescence excitation (PLE), and decay curves were measured by the FLS980 spectrometer (Edinburgh Instruments, the United Kingdom), The ML spectrum is measured by the coupling measurement of the stretching circulatory system of the Ocean Insight (QE-Pro) and Mechanics Experimental Machine. The cyclic photon experiment is measured by the stretching system of the mechanical experiment machine (Force-10 N, Speed-12 mm $s^{-1}$) and the Photon Detection Unit (C13796) connected to the optical fiber. All test photos and data for stability and weather resistance are taken through the continuous shooting mode of the Nikon D7500 and tested by the coupling of the friction tester and the QE-Pro. The triboelectric properties were detected through the CSM friction testing machine (Tribometer 3, Switzerland) equipped with an electrostatic measuring probe (SK050, KEYENCE (Japan) Co., Ltd.). The distance from the friction interface to the electrostatic measuring probe is fixed at 10 cm, and the CSM friction machine adopts a rotating module with a rotation radius of 3 mm and a speed of 60 rpm. Static electricity luminescence (SEL) is measured at a fixed distance by an electrostatic generator gun (GC90, Green techno Co., Ltd., Kanagawa, Japan) at a voltage of 1–10 KV and a fixed voltage of 5 KV. The TD-3000 diffractometer (Cu–Ka) is used as the X-ray light source in all X-ray (RL) tests. The emitted X-ray wavelength is $\lambda$ = 0.15 405 nm. For the thermoluminescence (2D/3D-TL) measurements, the samples were mounted on a thermal stage (298-650 K, LTTL-3DS, Radi Tec), after irradiation with 365 nm UV light or high-energy X-Ray/SE for 3 min, the heating rate was 1 K $s^{-1}$ and reached 600 K. Sample morphology was measured by using a scanning electron microscope TESCAN VEGA 3 SEM (Tescan China, Ltd.). Energy-dispersive spectrum (EDS) and element mapping (MAPPING) were obtained by using Table electron microscopy.

*Friction Test*: The mechanical behavior was carried out using a friction testing machine (MS-T3001) and the ML signals were collected in situ via a fiber spectrometer (QE Pro, Ocean Optics). Specifically, the ML materials were compounded with PDMS at a ratio of 1:2, and the compounded material was then placed in a mold and dried at 80 °C for 2 h. For the friction experiments, different weights were placed on top of the friction pair to adjust the load variations. During the friction process, dynamic spectra were captured using marine optical instruments with an integration time of 1 s.

*Strain Test*: The strain experiment was conducted using a tensile testing machine with a 100N pneumatic fixture attachment, with a tensile travel strain of 0–100%, a gauge length of 20 mm, and a tensile speed of 16.6 mm $s^{-1}$. In addition, for the syringe pressure test, a composite device of ≈755 µm was placed on the top of the syringe, and the test was taken by manually pushing and squeezing. All dynamic spectra were collected by Ocean Optics QE-Pro with an integration time of 300 ms.

*First-Principles Calculation*: The density functional theory (DFT) method implemented in the Vienna Ab initio Simulation Package (VASP) was employed for first-principles calculations concerning the structural optimization and electronic structure determination of both pure $Ca_3(PO_4)_2$ and Mn-doped $Ca_3(PO_4)_2$.[33] The convergence criteria for total energy and forces were set to be less than $10^{-5}$ eV and $10^{-2}$ eV $Å^{-1}$, respectively, with a plane-wave energy cutoff of 500 eV. The Perdew-Burke-Ernzerhof (PBE) functional within the generalized gradient approximation (GGA) and projected augmented wave (PAW) potentials were utilized to characterize the electron exchange-correlation energy and the interactions between valence electrons and ionic nuclei.[34,35] In the investigation of Mn-doped $Ca_3(PO_4)_2$, a Γ point mesh containing 276 atoms was employed for electronic structure sampling, with an Mn-to-Ca atom ratio of 1:65, corresponding to a doping concentration of 1.5%. A $2 \times 2 \times 1$ supercell was utilized to model Mn-doped $Ca_3(PO_4)_2$, resulting in optimized lattice parameters of $a = 10.41$ Å, $b = 10.41$ Å, and $c = 37.18$ Å.

## Supporting Information

Supporting Information is available from the Wiley Online Library or from the author.

## Acknowledgements

This work was supported by the National Natural Science Foundation of China (Grant No. 52173214), the Youth Innovation Team of Shaanxi Universities (No. 2022-70), the Youth Innovation Team Project of Shaanxi Province (23JP018), Natural Science Foundation of Shaanxi Province of China (NO. 2024JC-YBMS-042) and The Youth Innovation Team of Shaanxi Universities.

## Conflict of Interest

The authors declare no conflict of interest.

## Data Availability Statement

The data that support the findings of this study are available in the supplementary material of this article.

## Keywords

mechanoluminescence, pressure sensing, ratiometric, trap

Received: July 19, 2024
Revised: August 20, 2024
Published online:

[1] J. C. Zhang, X. S. Wang, G. Marriott, C. N. Xu, *Prog. Mater. Sci.* **2019**, *103*, 678.
[2] C. N. Xu, T. Watanabe, M. Akiyama, X. G. Zheng, *Appl. Phys. Lett.* **1999**, *74*, 2414.
[3] Y. J. Zhao, G. X. Bai, Y. Q. Huang, Y. Liu, D. F. Peng, L. Chen, S. Q. Xu, *Nano Energy* **2021**, *87*, 106177.
[4] Y. Lee, J. Park, A. Choe, S. Cho, J. Kim, H. Ko, *Adv. Funct. Mater.* **2020**, *30*, 1904523.
[5] C. F. Wang, D. F. Peng, C. Pan, *Sci. Bull.* **2020**, *65*, 1147.
[6] Y. T. Zheng, X. Li, R. H. Ma, Z. F. Huang, C. F. Wang, M. J. Zhu, Y. Y. Du, X. Chen, C. F. Pan, B. H. Wang, Y. Wang, D. F. Peng, *Small* **2022**, *18*, 2107437.
[7] C. Y. Jia, Y. F. Xia, Y. Zhu, M. Wu, S. L. Zhu, X. Wang, *Adv. Funct. Mater.* **2022**, *32*, 2201292.
[8] Q. Q. Zhou, Z. X. Geng, L. Yang, B. Shen, Z. T. Kan, Y. Qi, S. T. Hu, B. Dong, X. Bai, L. Xu, H. W. Song, L. Q. Ren, *Adv. Sci.* **2023**, *10*, 2207663.
[9] R. S. Andre, L. A. Mercante, M. H. M. Facure, R. C. Sanfelice, L. Fugikawa-Santos, T. M. Swager, D. S. Correa, *A. C. S. Sens.* **2022**, *7*, 2104.
[10] J. C. Zhang, X. Y. Xue, Y. F. Zhu, S. S. Wang, H. W. He, X. Yan, X. Ning, D. Wang, J. R. Qiu, *Chem. Eng. J.* **2021**, *406*, 126798.
[11] Y. X. Zhuang, D. Tu, C. J. Chen, L. Wang, H. W. Zhang, H. Xue, C. H. Yuan, G. R. Chen, C. F. Pan, L. Z. Dai, R. J. Xie, *Light Sci. Appl.* **2020**, *9*, 1.
[12] Y. L. Yang, X. C. Yang, J. Y. Yuan, T. Li, Y. T. Fan, L. Wang, Z. Deng, Q. L. Li, D. Y. Wan, J. T. Zhao, Z. J. Zhang, *Adv. Opt. Mater.* **2021**, *9*, 2100668.
[13] B. Chen, X. Zhang, F. Wang, *Acc. Mater. Res.* **2021**, *2*, 364.
[14] S. Zhou, Y. Cheng, J. Xu, H. Lin, Y. Wang, *Adv. Funct. Mater.* **2022**, *32*, 2208919.
[15] S. Wu, P. X. Xiong, D. L. Jiang, B. L. Xiao, Y. Xiao, Y. Chen, Y. Z. Wang, *Chem. Eng. J.* **2023**, *469*, 143961.
[16] C. J. Chen, Y. X. Zhuang, X. Y. Li, F. Y. Lin, D. F. Peng, D. Tu, A. Xie, R. J. Xie, *Adv. Funct. Mater.* **2021**, *31*, 2101567.
[17] Y. J. Zhao, D. F. Peng, G. X. Bai, Y. Q. Huang, S. Q. Xu, J. H. Hao, *Adv. Funct. Mater.* **2021**, *31*, 2010265.
[18] B. R. Tian, Z. F. Wang, A. T. Smith, Y. Q. Bai, J. Z. Li, N. Zhang, Z. H. Xue, L. Y. Sun, *Nano Energy* **2021**, *83*, 105860.
[19] S. Zhou, Y. Cheng, J. Xu, H. Lin, W. J. Liang, Y. S. Wang, *Laser Photonics Rev.* **2022**, *16*, 2100666.
[20] X. X. Yang, Y. Cheng, Z. C. Liu, J. Zhang, J. Xu, H. Lin, Y. S. Wang, *Laser Photonics Rev.* **2024**, *18*, 2301004.
[21] D. F. Peng, Y. Jiang, B. L. Huang, Y. Y. Du, J. X. Zhao, X. Zhang, R. H. Ma, S. Golovynskyi, B. Chen, F. Wang, *Adv. Mater.* **2020**, *32*, 1907747.
[22] F. L. Wang, F. L. Wang, X. D. Wang, S. C. Wang, J. F. Jiang, Q. L. Liu, X. T. Hao, L. Han, J. J. Wang, C. F. Pan, H. Liu, Y. H. Sang, *Nano Energy* **2019**, *63*, 103861.
[23] Y. Q. Bai, X. P. Guo, B. R. Tian, Y. M. Liang, D. F. Peng, Z. F. Wang, *Adv. Sci.* **2022**, *9*, 2203249.
[24] L. Lei, M. H. Yi, Y. B. Wang, Y. J. Hua, J. J. Zhang, P. N. Prasad, S. Q. Xu, *Nat. Commun.* **2024**, *15*, 1140.
[25] L. Lei, Y. B. Wang, W. X. Xu, R. G. Ye, Y. J. Hua, D. G. Deng, L. Chen, P. N. Prasad, S. Q. Xu, *Nat. Commun.* **2022**, *13*, 5739.
[26] X. Y. Ou, X. Qin, B. L. Huang, J. Zan, Q. X. Wu, Z. Z. Hong, L. L. Xie, H. Y. Bian, Z. G. Yi, X. F. Chen, Y. M. Wu, X. R. Song, J. Li, Q. S. Chen, H. H. Yang, X. G. Liu, *Nature* **2021**, *590*, 410.
[27] Y. Q. Tang, Y. Y. Cai, K. P. Dou, J. Q. Chang, W. Li, S. S. Wang, M. Z. Sun, B. L. Huang, X. F. Liu, J. R. Qiu, L. Zhou, M. M. Wu, J. C. Zhang, *Nat. Commun.* **2024**, *15*, 3209.
[28] M. Y. Wang, H. Wu, W. B. Dong, J. Y. Lian, W. X. Wang, J. Y. Zhou, J. C. Zhang, *Inorg. Chem.* **2022**, *61*, 2911.
[29] X. D. Wang, H. L. Zhang, R. M. Yu, L. Dong, D. F. Peng, A. H. Zhang, Y. Zhang, H. Liu, C. F. Pan, Z. L. Wang, *Adv. Mater.* **2015**, *27*, 2324.
[30] S. J. Kim, F. Yang, H. S. Jung, G. S. Hong, S. K. Hahn, *Adv. Funct. Mater.* **2024**, *34*, 2314861.

[31] Y. M. Song, Y. Y. Li, Z. B. Chen, G. T. Zhang, A. N. Yakovlev, T. T. Hu, T. G. Cherkasova, X. H. Xu, L. Zhao, *Ceram. Int.* **2023**, *49*, 30685.
[32] Y. X. Zhuang, X. Y. Li, F. Y. Lin, C. J. Chen, Z. S. Wu, H. D. Luo, L. B. Jin, R. J. Xie, *Adv. Mater.* **2022**, *34*, 2202864.
[33] G. Kresse, J. Furthmüller, *Phys. Rev. B.* **1996**, *54*, 11169.
[34] G. Kresse, D. Joubert, *Phys. Rev. B.* **1999**, *59*, 1758.
[35] J. P. Perdew, K. Burke, M. Ernzerhof, *Phys. Rev. Lett.* **1996**, *77*, 3865.